Enriched vacancies of ruthenium doped niobium oxide on hollow graphene sphere as sulfur reduction reaction promoter in lithium sulfur batteries

Rongrong Chu [a], Thanh Tuan Nguyen [a], Hewei Song [a], Yanqun Bai [a], Duy Thanh Tran [a], Nam Hoon Kim [a],[*], Joong Hee Lee [a],[b],[**]

[a] Department of Nano Convergence Engineering, Jeonbuk National University, Jeonju, Jeonbuk 54896, Republic of Korea
[b] Carbon Composite Research Centre, Department of Polymer – Nano Science and Technology, Jeonbuk National University, Jeonju, Jeonbuk 54896, Republic of Korea

ARTICLE INFO

ABSTRACT

Inhibiting the shuttle effect of soluble polysulfides (LiPSs) is critical to lithium–sulfur (Li–S) batteries. Nevertheless, the conventional separator fails to block immigration of LiPSs between electrodes. Herein, the enriched oxygen vacancies were stabilized with ruthenium doping on niobium oxide/three-dimensional reduced graphene oxide nanosphere (Nb_2O_{5-x}/Ru-3DG) to prepare a functional separator layer for LiPSs diffusion prevention. The inhibition mechanism is unraveled by density functional theoretical calculations and experimental results. Li–S batteries with Nb_2O_{5-x}/Ru-3DG-based separator displayed an excellent capacity of 700.3 mAh g^{-1} with a long-term stability of 1000 cycles and a high rate-performance of 533.2 mAh g^{-1} at 8 C. An industrial-level pouch cell delivered an outstanding specific capacity of 925.8 mAh g^{-1} with an exceptional flexibility. This study could open a new strategy to design materials with controlled defects and doping for LiPSs immobilization, enhanced catalytic activities for redox reaction, and other catalysts for energy conversion and storage devices.

1. Introduction

Rapid growth of portable electronic devices and large-scale energy storages has led to a high demand for low-cost and high-energy density rechargeable batteries. Lithium–sulfur (Li–S) batteries are recognized as one of the most compelling candidates for energy storage devices with the above requirement owing to their impressive theoretical energy density (2600 Wh kg^{-1}) and excellent theoretical capacity (1675 mAh g^{-1}) [1,2]. Nevertheless, practical applications of the state-of-the-art Li–S batteries are inhibited by a series of challenging problems from sulfur cathode and lithium anode. For example, the insulating nature of sulfur and final discharge product (Li_2S) can hold up the electron transport during the redox reaction that can cause inefficient sulfur use and sluggish LiPSs conversion kinetics [3–5]. Moreover, accomplished dissolution of LiPSs in electrolyte can result in diffusion between electrodes (shuttling effect), giving rise to anode deterioration and rapid capacity decay [6,7]. As a consequence, a well-organized strategy to stabilize the LiPSs and accelerate the transformation reaction kinetics is highly essential.

The separator is an important part of the battery that distinct the electron transport between the cathode and the anode to avoid short circuit. However, it cannot inhibit the immigration of LiPSs. A modified separator with an active coated layer could not only effectively entrap the LiPSs and prevent the diffusion into an electrolyte, but also accelerate the transformation reaction kinetics for enhancing sulfur utilization [8]. Till now, various materials have been developed to construct modified separators and establish functional electrode-separator interfaces for Li–S batteries. In particular, carbon-based materials (i.e., biomass carbon [9,10], carbon nanotubes [11–13], porous carbon [14–18], graphene [19,20], etc) are commonly considered for a coating layer for physical LiPSs immobilization due to their inexpensiveness, high electrical conductivity, and large specific surface area. Nevertheless, the nonpolar nature of carbon-based materials can only generate a weak van der Waals interaction with polar LiPSs, leading to incompetent stabilization. To better inhibiting the LiPSs shuttling effect, polar based materials that could generate a strong chemical bonding and boost the reaction kinetics can be used for an active layer [21,22]. Polar metal compounds such as metal oxide that can be used to make a helpful active layer to immobilize LiPSs by strong chemical adsorption binding have received extensive attention [23–26]. However, they have limitations

---

such as constraint of active sites, low electrical conductivity, and unsatisfied catalyst activities that might affect LiPSs attachment and low sulfur utilization [27]. Therefore, materials with excellent electrical conductivity and numerous active sites are needed to enhance LiPSs immobilization and transformation reaction kinetics.

Imperfections of crystal and functional defects play an important role in controlling various material properties by redistributing local electron and exposing plentiful coordinative unsaturated sites [28–32]. Oxygen vacancies (OVs) are recognized as general defects which could stimulate the benefit of a metal oxide such as transforming an oxide insulator into a metal conductor [33,34], prompting superconductivity properties [35], boosting catalyst activities [36], and enhancing ion conductivity [37]. Manipulating OVs is rising as a promising strategy to obtain desired functional properties of materials for Li–S batteries, supercapacitors, lithium-ion batteries, and electrochemical catalysis [38–41]. For example, Wang et al. have revealed a defect engineering procedure to develop WO@NC, which has abundant active sites and high surface binding energy to inhibit dissolution and promote redox conversion of LiPSs [42]. Ma and co-workers designed a high-performance anatase/rutile-TiO_2 electrocatalyst with enriched oxygen vacancies that could improve the immobilization and boost the catalytic conversion of LiPSs [43]. On the other hand, noble metal doping can effectively regulate intrinsic properties of host, optimize material utilization, and generate numerous defects for enhanced electrochemical performance [44]. In addition, doping of a noble metal to a transition metal oxide could stabilize oxygen vacancies and lead to a synergistic effect between dual active sites, therefore improving reaction kinetics [45].

Herein, we successfully fabricated a ruthenium-doped niobium oxide nanostructure with enriched oxygen vacancies anchored on three-dimensional graphene (Nb_2O_{5-x}/Ru-3DG) via a two-step strategy with facile hydrothermal and controlled annealing methods. The enriched oxygen vacancies were systematically designed and maximized to promote the redox reaction kinetics. Moreover, the incorporation of small amount of Ru atom not only prevents the overuse of expensive elements but also enlarges the active sites and modulates the electronic configuration. Doping of Ru atoms could immobilize oxygen vacancies at Nb_2O_{5-x} crystal by compensating the coordination number and further modulating electronic properties of catalyst. The mechanism for enhanced electrochemical performance was systematically investigated and examined. When serving as the coating layer for modified separator, batteries displayed excellent catalytic activities and adsorption capacity with outstanding electrochemical performance. As a result, Nb_2O_{5-x}/Ru-3DG modified separators-based Li–S coin-cell exhibited a remarkable initial capability of 933.7 mAh g^{-1} with an unprecedented cycling stability and an ultra-low capacity fading of 0.025% per cycle at 2.0 C over 1000 cycles. More impressively, the industrial-scale pouch-cell showed an outstanding specific capacity of 925.8 mAh g^{-1} at a high sulfur loading of 4.2 mg cm^{-2}, which could provide high competence for alternative energy storage devices toward benchmark Li-ion batteries.

2. Experimental section

2.1. Preparation of polystyrene spheres (PS)

Typically, stabilized styrene (7 mL, Sigma-Aldrich) was washed with 10 wt% NaOH solution (2 mL, Daesung Chem) to remove the stabilizer. The as-washed styrene was then added into a triple-neck flask with 50 mL water containing 0.25 g polyvinylpyrrolidone (PVP, Mw = 30,000). After that, the mixture was purged with high purity N_2 gas for 20 min followed by stirring at 75 ℃ for 30 min under a rotation speed of 700 rpm. Then 0.1 g $K_2S_2O_8$ in 5 mL water solution was added into the flask and the reaction was kept for 24 h with constant stirring to obtain a milk-like colloidal. PS products were collected by washing several times with deionized water and dried at 60 ℃ overnight.

2.2. Preparation of Nb_2O_{5-x}/Ru-3DG

Graphene oxide (GO) was synthesized using the modified Hummers' method [46]. Next, 90 mg of GO and 450 mg of PS were added into 100 mL of ultrapure water, followed by vigorously stirring for 5 h. Then 10 mg of $RuCl_3.xH_2O$ was added to 10 mL water/ethanol solution (v/v = 1:1) containing 150 mg $NbCl_5$. After that, the mixture was injected into PS/GO solution and kept stirring for 2 h. The precursor was obtained by freeze drying for 3 days at –80 ℃. Subsequently, the solid powder was annealed in a tube furnace at 650 °C for 2 h under heating rate of 5 °C min^{-1} and Ar/H_2 (v/v=95/5) atmosphere to obtain Nb_2O_{5-x}/Ru-3DG. For comparison, Nb_2O_5/Ru-3DG and Nb_2O_5-3DG were prepared using a similar method without H_2 and $RuCl_3.xH_2O$, respectively.

2.3. Preparation of Nb_2O_{5-x}/Ru-3DG, Nb_2O_5/Ru-3DG, or Nb_2O_5-3DG modified separator

Firstly, a slurry was prepared by dispersing 80 mg Nb_2O_{5-x}/Ru-3DG, 10 mg carbon black (CB), and 10 mg polyvinylidene fluoride (PVDF) binder in N-methyl-2-pyrrolidone (NMP) solvent followed by vigorous stirring. Subsequently, the as-obtained slurry was coated on a clean PP separator with a doctor blade to obtain a modified separator, which was then dried at 60 ℃ overnight under vacuum. After drying, the modified separator was punched into 1.9 cm diameter discs. The average mass loading of materials was measured to be about 0.32 mg cm^{-2}. For comparison, Nb_2O_5/Ru-3DG and Nb_2O_5-3DG coated separators were prepared using a similar procedure with the same mass loading.

2.4. Electrochemical measurements

CNT/S composite was first prepared using a melt diffusion method. A commercial CNT was uniformly ground and mixed with sublimed sulfur at a weight ratio of 1:4. The mixture was then sealed under Ar atmosphere and heated at 155 ℃ for 8 h. The obtained CNT/S composite was further mixed with 10% CB and PVDF binder and dispersed in NMP solvent to form a slurry. The homogenous slurry was coated on an aluminum foil using a doctor-blade and dried at 80 °C overnight under vacuum condition. As electrolyte, 1.0 M solution of bis(trifluorome) sulfonimide lithium salt (LiTFSI) (99.95% trace metals basis) in dimethoxyethane (DME) and 1,3-dioxolane (DOL) (v/v = 1:1) with 1 wt% lithium nitrate ($LiNO_3$) was used. Li foil and Nb_2O_{5-x}/Ru-3DG, Nb_2O_5/Ru-3DG, or Nb_2O_5-3DG modified PP were used as anode and separator, respectively. Electrochemical tests were performed by assembling CR2032 coin cell configuration in an Ar filled glovebox where oxygen and moisture contents were less than 0.1 ppm. Galvanostatic charge-discharge measurements were carried out with a Maccor instrument (Series 400 automated test system) at a voltage window of 1.5–3.0 V under various scan rates. Cyclic voltammetry (CV) and electrochemical impedance spectroscopy (EIS) curves were performed within a Gamry electrochemical workstation. CV was tested at scan rate of 0.1–0.5 mV s^{-1} and EIS was obtained at a frequency range from 10 mHz to 100 kHz.

2.5. Visualized adsorption of Li_2S_6

Li_2S_6 solution was selected to characterize visual adsorption of all materials. Sulfur and Li_2S were mixed at a stoichiometric ratio of 5:1 into a mixture of DOL and DME (v/v = 1:1) with continuous stirring overnight under Ar atmosphere. Samples were then added separately into 3.0 mL of Li_2S_6 solutions and kept standing without disturbance. After 6 h, supernatants and precipitates were collected for further characterization.

2.6. Symmetrical cell assembly and measurements

Working electrodes for symmetric cells were prepared by mixing

active materials (Nb$_2$O$_{5-x}$/Ru-3DG, Nb$_2$O$_5$/Ru-3DG, Nb$_2$O$_5$-3DG) and PVDF binder at a mass ratio of 9:1 in NMP, followed by coating the homogeneous slurry onto aluminum foil. Coated samples were dried and punched (16 mm in diameter) for each electrode. Cells were assembled with two identical electrodes as both working and counter electrodes. A 0.5 M Li$_2$S$_6$ in DOL/DME (v/v = 1:1) containing 1 M LiTFSI was used as electrolyte. CV measurements of symmetric cells were performed at various scan rates ranging from 5 to 25 mV s^{-1} at a voltage range of -0.9 to 0.9 V (vs. Li/Li$^+$).

2.7. Li$_2$S nucleation test

As-prepared materials were coated on carbon paper and employed as working electrodes with Li foil as counter electrodes. Li$_2$S$_8$ electrolyte was prepared by mixing sulfur and Li$_2$S (molar ratio 7:1) in a mixture of DOL/DME (v/v = 1:1) followed by constant stirring for 4 h. During coin cell assembly, 20 μL of Li$_2$S$_8$ catholyte was added. Cells were galvanostatically discharged to 2.06 V at a current of 0.112 mA and held potentiostatically at 2.05 V for Li$_2$S nucleation until the current gradually reduced to 0.01 mA.

3. Results and discussion

The preparation procedure of Nb$_2$O$_{5-x}$/Ru-3DG is shown in Fig. 1. The PS was chosen as a soft template for hollow 3DG growth. It also could serve as a framework for Nb^{5+} and Ru^{3+} ions dispersion. After stirring for several hours, PS/GO-salt composites in powder form were obtained by freeze-drying. Finally, the Nb$_2$O$_{5-x}$/Ru-3DG product was sintered under Ar/H$_2$ atmosphere. During a heat treatment process, the PS was decomposed, and GO was reduced to form a stable 3DG with a uniform dispersion of Nb$_2$O$_{5-x}$/Ru-3DG. On another hand, we prepared materials with similar procedure without PS template for comparison. Morphology and internal nanostructure of as-prepared materials were

then characterized using a scanning electron microscope (SEM) and a transmission electron microscope (TEM). The PS template showed a uniform size and a smooth spherical structure, which could be a suitable template for formation of Nb$_2$O$_{5-x}$/Ru-3DG (Fig. S1). Fig. S2 exhibited the PS/GO-salt composites with well-interaction between GO and PS template after free-drying process. Under pyrolysis process, the PS was decomposed, and a well-defined 3D interconnected hollow nano-structure was obtained (Fig. 2a-b and Fig. S3). This novel 3D structure can provide enough space and pore size for LiPSs immobilization and effectively improve electronic conductivity to facilitate electron transport [47]. TEM image shown in Fig. 2c revealed that the average diameter of hollow spheres was around 240 nm, well-consistent with PS template and SEM image. Thin layers of rGO nanosheets were completely wrapped with a wrinkly surface as shown in Fig. 2c. High-resolution TEM (HR-TEM) image displayed high crystallinity and clearly revealed lattice structures of the Nb$_2$O$_{5-x}$/Ru-3DG composite (Fig. 2d). As shown in Fig. 2e-f, the lattice distance presented a value of 0.31 nm which was related to the (001) facet of Nb$_2$O$_5$. Besides, numerous defects were observed as shown in blue circles of Fig. 2e, indicating successful formation of oxygen vacancies in Nb$_2$O$_{5-x}$/Ru-3DG. Moreover, the height profile shown in Fig. 2f and the obvious bright spot in Fig. 2h illustrated variation, further proving the successful O vacancy formation with doping of Ru atoms into Nb$_2$O$_{5-x}$ nano-structures. Fig. 2g shows various species of Nb$_2$O$_{5-x}$/Ru dispersed on the hollow 3DG nanosphere. Inset of Fig. 2g shows polycrystalline diffraction rings in selected area electron diffraction pattern (SAED) analysis, which were ascribed to (182), (002), (181), (180), and (001) planes of Nb$_2$O$_5$ [48]. Line mapping in Fig. 2i demonstrated the Nb$_2$O$_{5-x}$/Ru species with higher intensity signals on the surface of the hollow 3DG nanosphere. In addition, uniform distributions of C, O, Nb and Ru elements were further demonstrated in EDS color-mapping analysis shown in Fig. 2j. Furthermore, Fig. S4 showed the materials that were synthesized without PS template, illustrating the two-dimensional
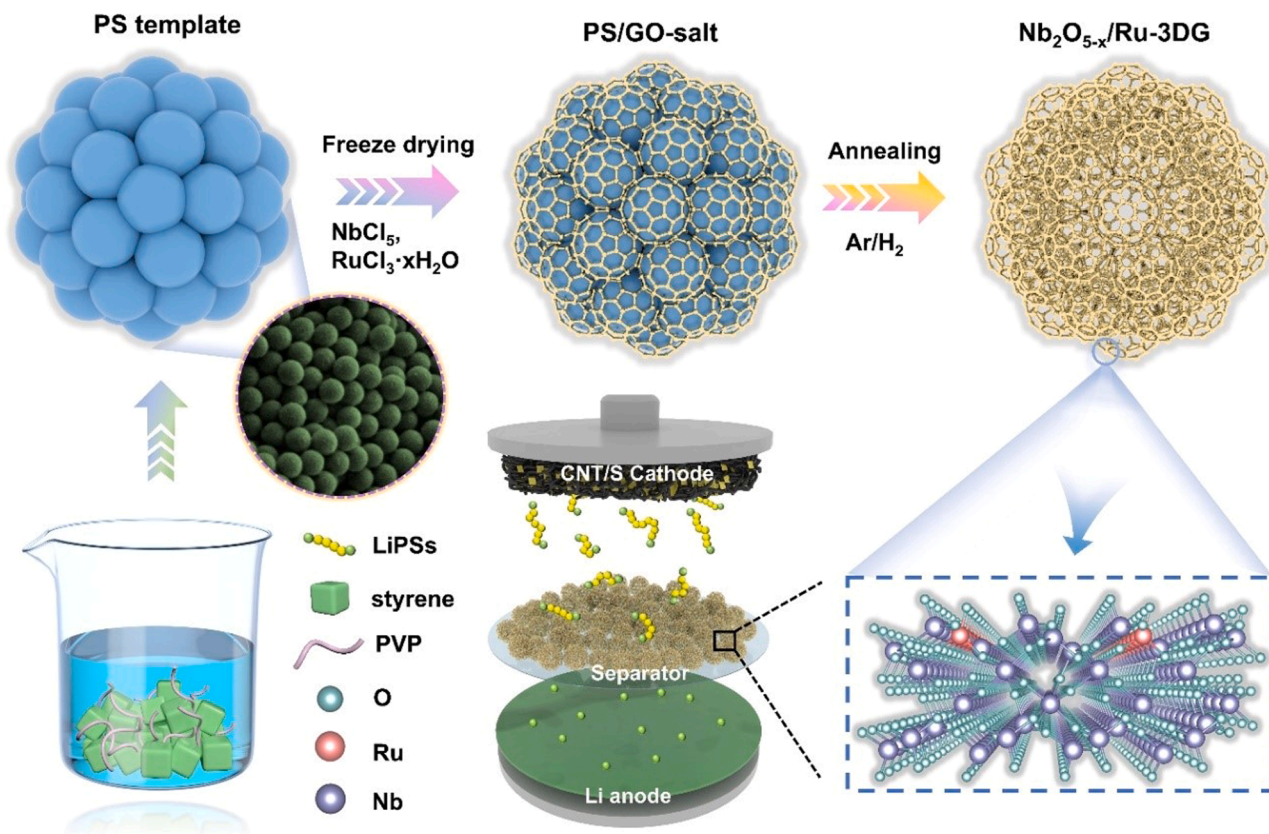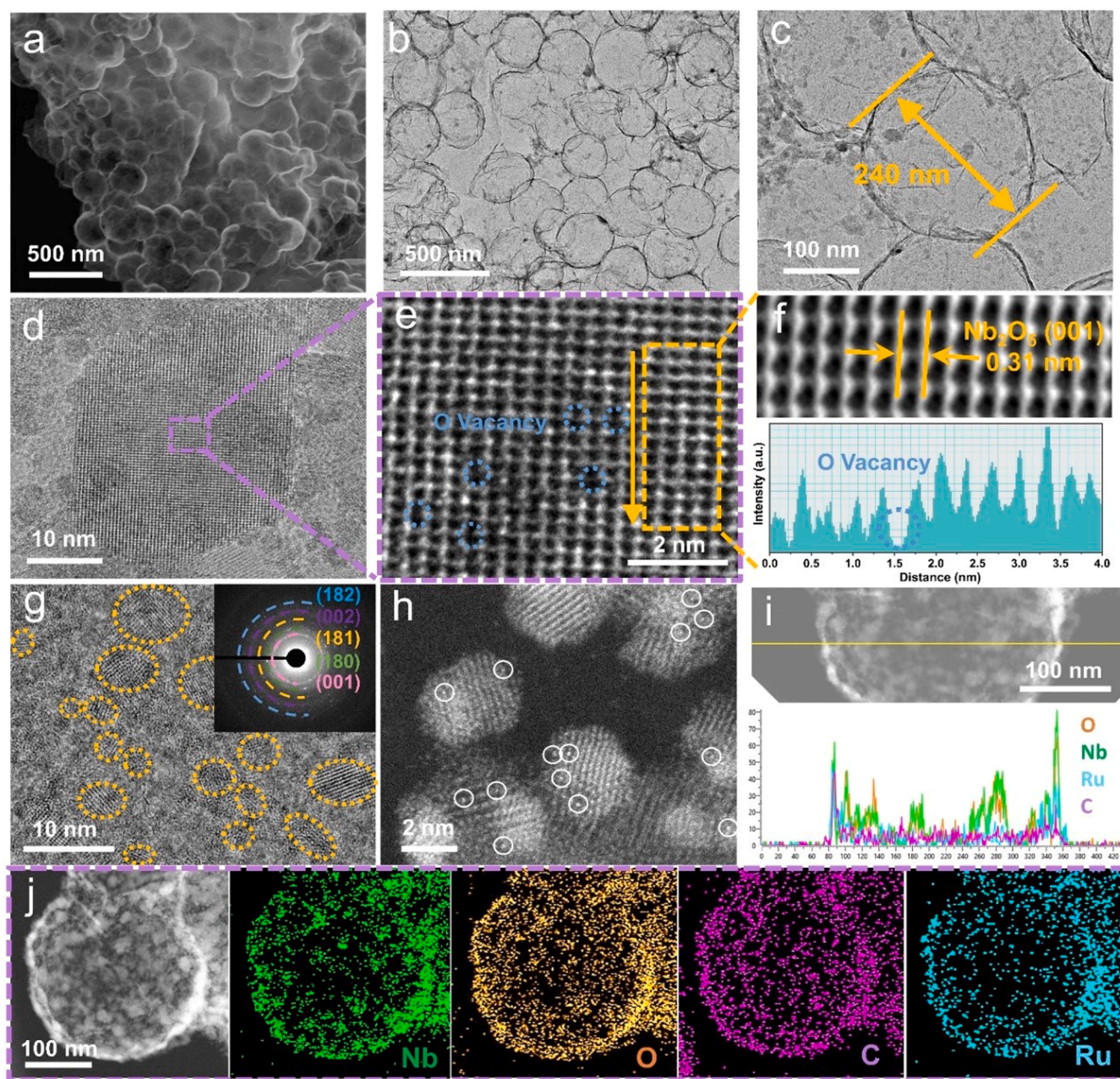

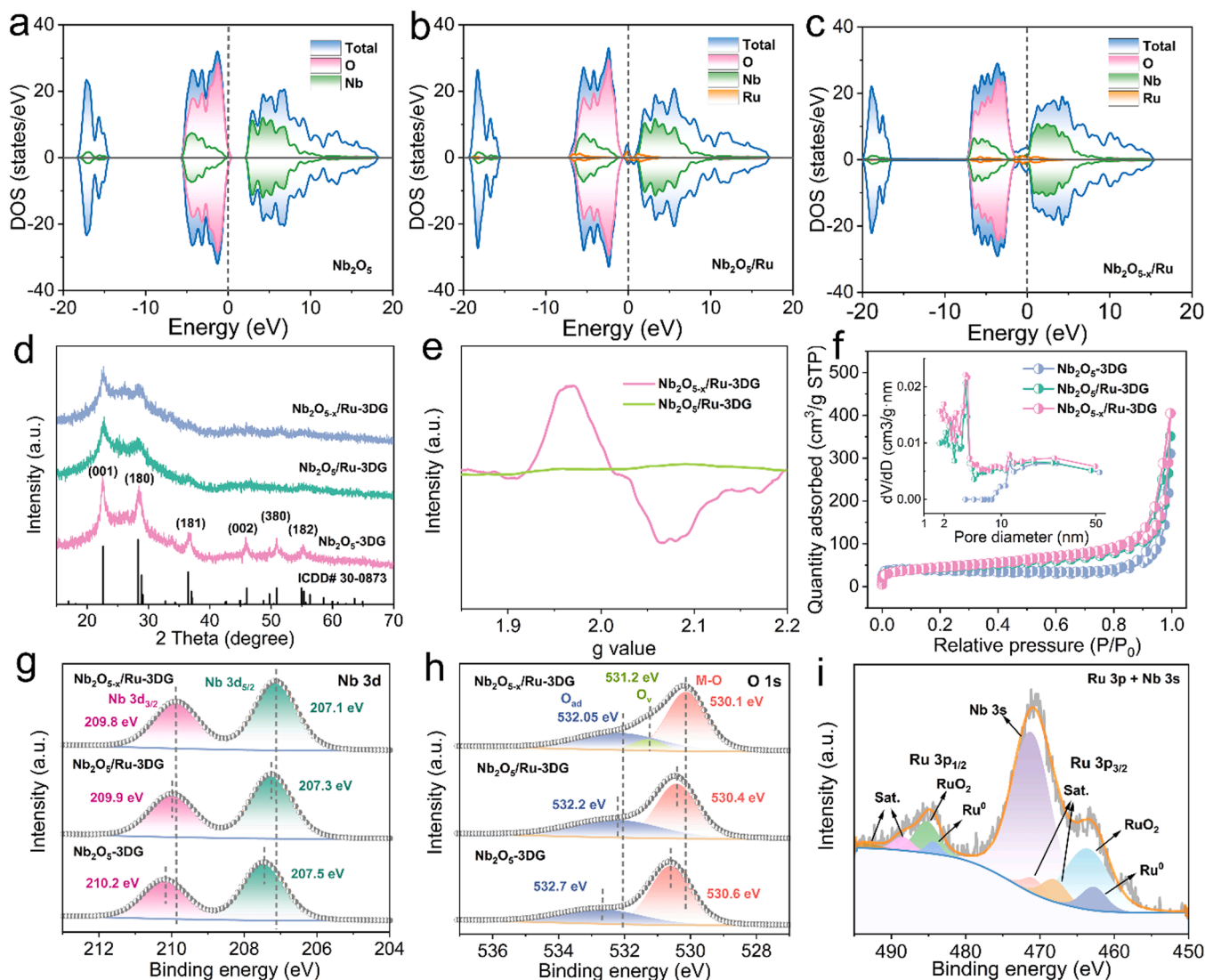**Fig. 1.** (a) Schematic illustration of the synthesis procedure of Nb$_2$O$_{5-x}$/Ru-3DG.

Fig. 2. (a) SEM image. (b) and (c) TEM images. (d) HRTEM images of Nb_2O_{5-x}/Ru-3DG. (e,f) Lattice spacing at selected areas and height profile of Nb_2O_{5-x}/Ru-3DG. (g) HR-TEM image with different Nb_2O_{5-x}/Ru sites (inset showed the SAED pattern). (h) STEM image. (i) Line mapping EDS. (j) Color mapping EDS with different elements of Nb_2O_{5-x}/Ru-3DG.

nanosheet nanostructure with layered and smooth surfaces.

Firstly, Nb_2O_5, Nb_2O_5/Ru, and Nb_2O_{5-x}/Ru models were built and DFT calculation was carried out to predict physical and electrochemical performance properties. The density of state (DOS) of a material at Fermi level can demonstrate the electron density which is associated with electrical conductivity of the model. As shown in Fig. 3a-c and Fig. S5, Nb_2O_{5-x}/Ru at Fermi level exhibited higher value of DOS than Nb_2O_5 and Nb_2O_5/Ru, suggesting its electron transport enhancement. Moreover, the charge density difference was performed and exhibited in Fig. S6 to examine the charge redistribution. The optimized structures show yellow and blue regions that represent charge accumulation and depletion, respectively. It can be observed that the generation of oxygen vacancies and Ru doping could cause distortion of electron distribution. In particular, the charge density difference in 2D views demonstrates the increasing in accumulation around Nb atoms that nearby the vacancy's

sites of Nb_2O_{5-x}/Ru, resulting the enhanced catalytic activities kinetic toward LiPS conversion reactions (Fig. S6b). Additionally, the theoretical work function for as-built models were calculated and exhibited in Fig. S7. The work function of Nb_2O_{5-x}/Ru showed a small value of 4.76 eV, that is lower than other counterparts of Nb_2O_5/Ru (5.26 eV) and Nb_2O_5 (7.24 eV), respectively. The smaller value of work function for Nb_2O_{5-x}/Ru demonstrates the reduced activation barrier and high catalytic activities of materials. Based on DFT results, we synthesized and analyzed samples with different configurations. The phase and crystallinity of all materials were described in X-ray diffraction (XRD) patterns. As shown in Fig. 3d, XRD patterns of Nb_2O_{5-x}/Ru-3DG, Nb_2O_5/Ru-3DG, and Nb_2O_5-3DG showed various diffraction peaks at around 22.5, 28.5 and 36.6°, which could be attributed to (001), (180), and (181) lattice planes of Nb_2O_5 (ICDD#30–0873), respectively. Similar peaks of all materials indicated that the introduction of small

Fig. 3. DOS calculation results for (a) Nb_2O_5, (b) Nb_2O_5/Ru, and (c) Nb_2O_{5-x}/Ru models. (d) XRD patterns. (e) EPR spectra. (f) N_2 adsorption/desorption isotherm curves of Nb_2O_{5-x}/Ru-3DG, Nb_2O_5/Ru-3DG, and Nb_2O_5-3DG (inset showing pore size distributions). High-resolution XPS of (g) Nb 3d and (h) O 1 s for Nb_2O_{5-x}/Ru-3DG, Nb_2O_5/Ru-3DG, and Nb_2O_5-3DG. And (i) Ru 3p and Nb 3 s for Nb_2O_{5-x}/Ru-3DG.

amount Ru heteroatoms and formation of O vacancies did not cause a phase transition. However, intensity decreased with a trend of Nb_2O_5-3DG > Nb_2O_5/Ru-3DG > Nb_2O_5/Ru due to doping of Ru and formation of O vacancies that could generate distortion, slight crystallinity degradation, and enhanced disorder of crystals [49]. In addition, broad peaks at 2θ of 25.5° corresponded to the typical peak of rGO. To further verify the existence of O vacancies in Nb_2O_{5-x}/Ru-3DG, we performed electron paramagnetic resonance (EPR) analysis for Nb_2O_{5-x}/Ru-3DG and Nb_2O_5/Ru-3DG, respectively. As shown in Fig. 3e, the Nb_2O_{5-x}/Ru-3DG exhibited a strong peak at the magnetic field corresponding to g = 2.003, indicating the generation of numerous O vacancies in the Nb_2O_{5-x}/Ru-3DG crystal. It might have been initiated from unpaired electrons of the anion species in Nb_2O_5 during Ar/H_2 annealing. The specific surface area and pore size nature of materials are important factors related to LiPSs adsorption ability. We performed Brunauer-Emmett-Teller (BET) nitrogen (N_2) adsorption/desorption test for all materials. Results are shown in Fig. 3f. Nb_2O_{5-x}/Ru-3DG composites exhibited a higher BET specific surface area of 204.8 $m^2 g^{-1}$ than Nb_2O_5/Ru-3DG (197.9 $m^2 g^{-1}$) and Nb_2O_5-3DG (168.4 $m^2 g^{-1}$), which was attributed to the introduction of Ru heteroatoms and sufficient defects from O vacancies. Furthermore, the inset of Fig. 3f demonstrates

pore size distribution of Nb_2O_{5-x}/Ru-3DG composite mainly driven by mesopores. The pore volume was as high as 0.065 $cm^3 g^{-1}$, which provided an efficient zone for LiPSs immobilization. The high pore volume of Nb_2O_{5-x}/Ru-3DG observed from Ru doping and O vacancies formation could generate abundant defects sites with enhanced porosity.
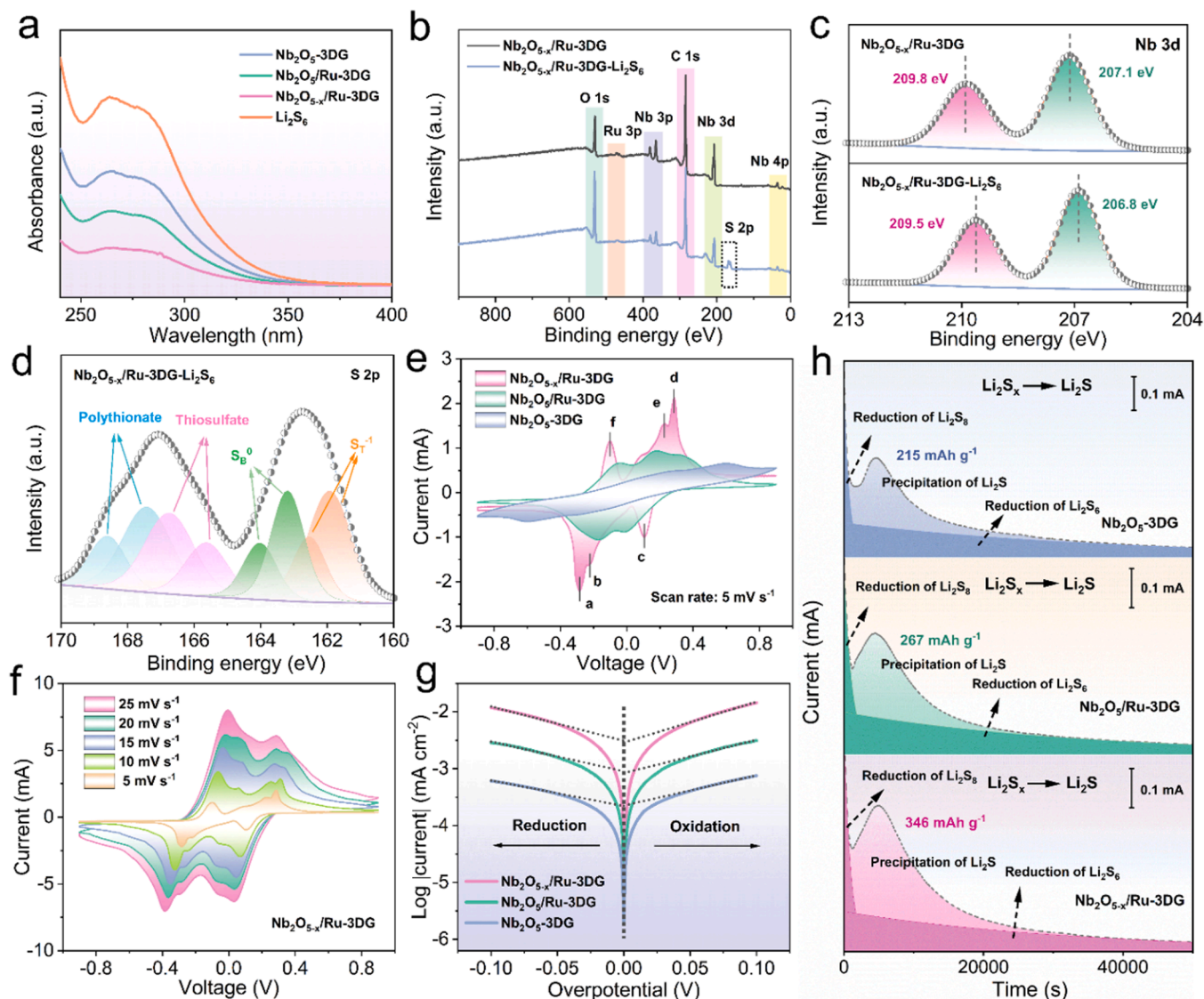
To further examine oxidation states and chemical compositions of all materials, X-ray photoelectron spectroscopy (XPS) analysis was carried out. Results of XPS analysis showed the existence of Nb, O, Ru, and C elements in Nb_2O_{5-x}/Ru-3DG. The high-resolution Nb 3d spectrum of Nb_2O_{5-x}/Ru-3DG was deconvoluted into two typical peaks at 209.8 and 207.1 eV assigned to Nb $3d_{3/2}$ and Nb $3d_{5/2}$, respectively, demonstrating the typical valence state of Nb^{5+} (Fig. 3g). Nb_2O_{5-x}/Ru-3DG and Nb_2O_5/Ru-3DG showed shifting to lower binding energy compared to pure Nb_2O_5-3DG owing to doping of Ru atom into Nb_2O_5 crystal and formation of O vacancies that manipulated electronic structures of materials. Fig. 3h exhibits XPS deconvolution of O 1 s for all materials. Typical peaks at binding energy ranges of 531.8–532.7 and 530.2–530.6 eV illustrated M-O and adsorption oxygen (O_{ad}). The appearance of additional peak at the binding energy of 531.2 eV indicated successful formation of O vacancies (O_v) in the Nb_2O_{5-x}/Ru-3DG

crystal. Moreover, the M-O peak of Nb_2O_{5-x}/Ru-3DG and Nb_2O_5/Ru-3DG gradually shifted to lower binding energy location compared to Nb_2O_5/3DG due to a doping effect. High-resolution XPS of Ru 3p + Nb 3 s showed a spinning couple of Ru located at binding energies of 463.6 and 485.3 eV indexed to Ru^{3+} $3p_{3/2}$ and Ru^{3+} $3p_{1/2}$, respectively (Fig. 3i) [50]. This result proved the Ru atom is in higher oxidation state and could enhance electrochemical activities. Moreover, small peak couples raised at binding energies of 462.7 and 484.3 eV assigned to small amount of metallic Ru.

The adsorption ability toward LiPSs of as-synthesized materials was examined using a visualized test. An appreciated amount of each material was added into separated vials with 5 mM Li_2S_6 solution. As shown in Fig. S8, the vial with Nb_2O_{5-x}/Ru-3DG was colorless after 5 h adsorption, demonstrating strong trapping of Li_2S_6. However, solutions with Nb_2O_5/Ru-3DG and Nb_2O_5-3DG materials remained a pale-yellow color owing to insufficient adsorption compared to Nb_2O_{5-x}/Ru-3DG. The solution was decanted for UV-Vis measurement and precipitation was collected for XPS. Fig. 4a presents UV–vis spectra of all materials after the adsorption test. The Li_2S_6 solution exhibited typical peaks at wavelengths of ~260 and 280 nm. Solutions with Nb_2O_5/Ru-3DG and

Nb_2O_5-3DG still showed some broad peaks, illustrating that Li_2S_6 remained after the test. In contrast, Li_2S_6 peaks almost disappeared in the solution with Nb_2O_{5-x}/Ru-3DG, proving an excellent adsorption ability.

To further determine chemical bonding and catalytic conversion effects of Nb_2O_{5-x}/Ru-3DG composites, XPS measurement was performed for Nb_2O_{5-x}/Ru-3DG before and after adsorption of LiPSs. After the adsorption test, the S 2p appeared on the survey XPS of Nb_2O_{5-x}/Ru-3DG-Li_2S_6, demonstrating successful binding with LiPSs (Fig. 4b). Moreover, the Nb 3d spectrum of the Nb_2O_{5-x}/Ru-3DG-Li_2S_6 showed down shifted binding energies of Nb $3d_{3/2}$ and Nb $3d_{5/2}$ peaks in comparison with Nb_2O_{5-x}/Ru-3DG due to a strong interaction between Nb_2O_{5-x}/Ru-3DG and Li_2S_6 species (Fig. 4c). The high-resolution Li 1 s spectrum of Nb_2O_{5-x}/Ru-3DG-Li_2S_6 exhibited two typical peaks located at binding energies of 55.2 and 56.1 eV assigned to Li-S and Li-O bonding, respectively (Fig. S9) [51]. The S 2p spectrum after Li_2S_6 adsorption displayed two obvious peaks at 163.1 and 161.8 eV, which could be ascribed to bridging sulfur (S_B^0) and terminal sulfur (S_T^{-1}), respectively. In addition, two characteristic peaks at 167.4 and 166.7 eV could be attributed to polythionate and thiosulfate species, respectively

Fig. 4. (a) UV vis of post-adsorption test solution for all materials. (b) XPS survey spectra of Nb_2O_{5-x}/Ru-3DG and Nb_2O_{5-x}/Ru-3DG-Li_2S_6. High-resolution XPS spectra of (c) Nb 3d and (d) S 2p in Nb_2O_{5-x}/Ru-3DG. (e) CV curves of Li_2S_6 symmetrical cells with Nb_2O_{5-x}/Ru-3DG, Nb_2O_5/Ru-3DG, and Nb_2O_5-3DG at 5 mV s^{-1}. (f) CV curves of Nb_2O_{5-x}/Ru-3DG symmetric cells at scan rates of 5–25 mV s^{-1}. (g) Tafel plots of symmetric cells. (h) Potentiostatic discharge curves of Li_2S nucleation.

(Fig. 4d). The formation of thiosulfate could be explained as a result of sulfur species oxidation in LiPSs. Furthermore, these generated thiosulfate species could combine with LiPSs to form polythionate and the final product (Li$_2$S) [52]. Therefore, the Nb$_2$O$_{5-x}$/Ru-3DG could play a critical role in immobilizing dissolved LiPSs and accelerating the redox reaction kinetics.
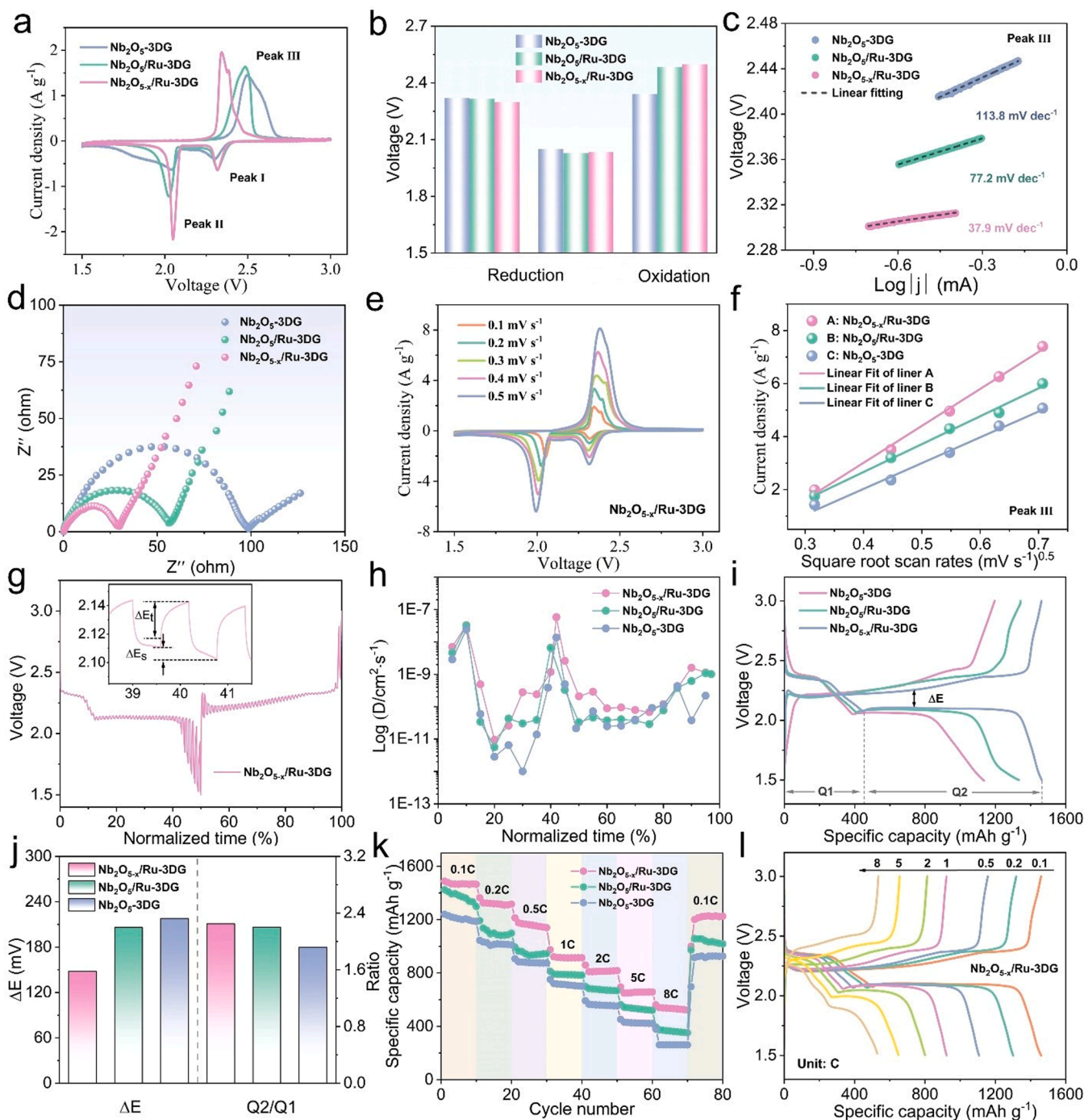
Transformation reaction kinetics of LiPSs can have a strong effect on the ability of shuttle effect inhibition and electrochemical performance of Li–S batteries. To investigate catalytic activities of Nb$_2$O$_{5-x}$/Ru-3DG, Nb$_2$O$_5$/Ru-3DG, and Nb$_2$O$_5$-3DG composites toward LiPSs conversion, symmetrical cells using the same electrode were assembled with Li$_2$S$_6$ as an electrolyte. As shown in Fig. 4e, CV profiles were recorded with different cells in the voltage range from −0.9 to 0.9 V at a scan rate of 5 mV s^{-1}. The Nb$_2$O$_{5-x}$/Ru-3DG electrode exhibited higher peak current response and lower polarization than Nb$_2$O$_5$/Ru-3DG and Nb$_2$O$_5$-3DG counterparts, indicating redox kinetics enhancement of Nb$_2$O$_{5-x}$/Ru-3DG for LiPSs conversion. Furthermore, CV profiles of Nb$_2$O$_{5-x}$/Ru-3DG based symmetric cell at different scan rates from 5–25 mV s^{-1} were obtained. Fig. 4f clearly showed a slight shift even at a higher CV scanning sweep, which was better than its counterparts of Nb$_2$O$_5$/Ru-3DG and Nb$_2$O$_5$-3DG (Fig. S10). These results confirmed the high reversibility of Nb$_2$O$_{5-x}$/Ru-3DG catalyst toward the transformation reaction that could enhance the conversion efficiency of LiPSs. The electrochemical impedance spectroscopy (EIS) was performed for symmetric cells, results are shown in Fig. S11. Nb$_2$O$_{5-x}$/Ru-3DG (42.24 Ω) showed lower charge transfer resistance than Nb$_2$O$_5$/Ru-3DG (59.32 Ω) and Nb$_2$O$_5$-3DG (116.57 Ω). The enhancement of charge transfer kinetics might have benefited from optimal design nanostructure of Nb$_2$O$_{5-x}$/Ru-3DG and distribution of O vacancies with Ru heteroatoms doping. Tafel plots were obtained to further confirm the electrocatalytic activity of Nb$_2$O$_{5-x}$/Ru-3DG towards LiPSs conversion (Fig. 4g). Tafel curves were fitted in the overpotential range of −0.1 ~ 0.1 V. The value of the exchange current density (I$_0$) was calculated from the Bulter–Volmer equation as shown below [53]:

$$\eta = a + b \times \log I \tag{1}$$

where the *a* is the constant, *b* is the Tafel slope, *η* is the overpotential, and *I* is the response current of symmetric cells. The Nb$_2$O$_{5-x}$/Ru-3DG exhibited the highest maximum I$_0$ during reduction and oxidation of 0.814 mA cm^{-2}, which outperformed Nb$_2$O$_5$/Ru-3DG (0.516 mA cm^{-2}) and Nb$_2$O$_5$-3DG (0.594 mA cm^{-2}). In addition, the lower Tafel slope value of Nb$_2$O$_{5-x}$/Ru-3DG based battery demonstrated an excellent catalytic ability for promoting conversion reaction kinetics.

During the charge/discharge process, LiPSs transformation undergoes numerous reactions and variable crystal formation from solid to liquid to solid. Precipitation of the final discharge product Li$_2$S plays a critical role in electrochemical performance of battery. It contributes to 3/4 total capacity of battery. Therefore, we further investigated nucleation and deposition of Li$_2$S on Nb$_2$O$_{5-x}$/Ru-3DG, Nb$_2$O$_5$/Ru-3DG, and Nb$_2$O$_5$-3DG to evaluate the ability of each material for LiPSs conversion. Potentiostatic discharge profiles for all materials are displayed in Fig. 4h. The specific deposition capacity of Li$_2$S nucleation was calculated according to the electron charge, which followed the Faraday's law [54]. As shown in Fig. 4h, the Li$_2$S precipitation capacity with Nb$_2$O$_{5-x}$/Ru-3DG based cell demonstrated the highest current response with an excellent nucleation capacity of 346 mAh g^{-1}, which was significantly higher than that of Nb$_2$O$_5$/Ru-3DG (267 mAh g^{-1}) or Nb$_2$O$_5$-3DG (215 mAh g^{-1}) based cells. Moreover, FE-SEM images of Li$_2$S deposition on Nb$_2$O$_{5-x}$/Ru-3DG, Nb$_2$O$_5$/Ru-3DG, and Nb$_2$O$_5$-3DG were obtained (Fig. S12). The Nb$_2$O$_{5-x}$/Ru-3DG based cell electrode exhibited uniform and abundant Li$_2$S precipitation, which was in flagrant contrast to severe uneven aggregation of Li$_2$S in Nb$_2$O$_5$/Ru-3DG and Nb$_2$O$_5$-3DG cell electrodes. These results further confirmed that Nb$_2$O$_{5-x}$/Ru-3DG had outstanding LiPSs conversion of that could promote Li$_2$S formation in comparison with its counterparts.

Fig. S13 shows FE-SEM image of pristine PP. It exhibited uniformly interwoven fishnet-like nanoscale pores visible on the surface that could easily let LiPSs immigrate through the membrane. In contrast, the Nb$_2$O$_{5-x}$/Ru-3DG composite with interlayer coated PP showed a uniformly layer with obvious pores to form a compatible channel for Li$^+$ migration. So, it suppressed the LiPSs with a strong adsorption ability (Fig. S14). In addition, the Nb$_2$O$_{5-x}$/Ru-3DG modified separator displayed excellent adhesion and flexible mechanical properties, which could avoid flaking or peeling after folding (Fig. S15). The FE-SEM image of Nb$_2$O$_{5-x}$/Ru-3DG modified separator in the cross-section view displayed a thickness of the interlayer of about 6 μm (Fig. S16a). Contribution of elements at the cross-section view is described in elemental color mapping shown in Fig. S16b, which exhibited a uniform distribution of C, O, Nb, and Ru. To investigate permeation resistance of Nb$_2$O$_{5-x}$/Ru-3DG toward LiPSs, we carried out an experiment using H-type cells with Nb$_2$O$_{5-x}$/Ru-3DG, Nb$_2$O$_5$/Ru-3DG, or Nb$_2$O$_5$-3DG based separators. As shown in Fig. S17, using H-cells with Nb$_2$O$_5$/Ru-3DG and Nb$_2$O$_5$-3DG based separators, more LiPSs penetrated from the cathode side to the anode side compared to the case of using Nb$_2$O$_{5-x}$/Ru-3DG based separators after 10 h, demonstrating an effective LiPSs blocking effect of Nb$_2$O$_{5-x}$/Ru-3DG by suppressing shuttling behaviors. To investigate the reduction and oxidation process of as-prepared Li–S batteries, we performed cyclic voltammetry (CV) analysis. As shown in Fig. 5a, the CV of Nb$_2$O$_{5-x}$/Ru-3DG based cells revealed two prominent cathodic peaks at 2.29 (peak I) and 2.04 V (peak II), which corresponded to the conversion of S to long-chain soluble LiPSs (Li$_2$S$_x$, $4 \leq x \leq 8$) and further to insoluble Li$_2$S/Li$_2$S$_2$. On the contrary, the anodic peak at 2.49 V (peak III) was associated with the reverse oxidation process from Li$_2$S/Li$_2$S$_2$ to S. Compared to Nb$_2$O$_5$/Ru-3DG and Nb$_2$O$_5$-3DG based cells, Nb$_2$O$_{5-x}$/Ru-3DG based cells exhibited the lowest oxidation potential and the highest reduction potential with a greater current density (Fig. 5b), suggesting that Nb$_2$O$_{5-x}$/Ru-3DG could effectively promote the electrochemical conversion of LiPSs. To evaluate the catalytic ability towards LiPSs transformation, the onset potential was derived and compared. The onset potential was estimated as the current above the baseline by 10 μA cm^{-2} (Fig. S18). Fig. S18e and Fig. S18f displayed the highest onset reduction potential and the lowest onset oxidation potential of Nb$_2$O$_{5-x}$/Ru-3DG based cells, which outperformed Nb$_2$O$_5$/Ru-3DG and Nb$_2$O$_5$-3DG based cells, demonstrating acceleration of redox kinetics and significantly reduced polarization during multistep phase transition. In addition, Tafel plots derived from CV profiles showed the lowest value of 37.9 mV dec^{-1} for Nb$_2$O$_{5-x}$/Ru-3DG based cells for oxidation process. Nb$_2$O$_{5-x}$/Ru-3DG based cells outperformed other controlled materials such as Nb$_2$O$_5$/Ru-3DG (Tafel value of 77.2 mV dec^{-1}) and Nb$_2$O$_5$-3DG (Tafel value of 113.8 mV dec^{-1}) based batteries (Fig. 5c). Similarly, for reduction processes, Nb$_2$O$_{5-x}$/Ru-3DG based cells showed low Tafel values of 58.6 and 18.8 mV dec^{-1} for peak I and peak II, respectively. These values were significantly smaller than those of Nb$_2$O$_5$/Ru-3DG (72.1 and 24.9 mV dec^{-1}) and Nb$_2$O$_5$-3DG (81.2 and 63.4 mV dec^{-1}) separators (Fig. S19). These results indicated an enhanced catalytic activity of Nb$_2$O$_{5-x}$/Ru-3DG which originated from the assistance of enriched O vacancies and Ru doping. To evaluate the charge transfer resistance of as-assembled cells, we performed EIS measurement at open circuit potential (OCP) (Fig. 5d). The Nb$_2$O$_{5-x}$/Ru-3DG based battery showed the lowest charge transfer resistance (Rct) of 29.05 Ω, which was smaller than the charge transfer resistance of Nb$_2$O$_5$/Ru-3DG (56.51 Ω) or Nb$_2$O$_5$-3DG (98.55 Ω) based cells. This result was due to the optimal structure of O vacancies and Ru doping that could increase charge transfer between electrode and electrolyte interface. The Li$^+$ diffusion coefficient is an important factor that demonstrates the transport ability of Li$^+$ which is necessary for chemical redox reaction. As proposed by Randles–Sevcik, the Li$^+$ diffusion coefficient could be estimated from CV analyses [55]. Thus, we carried out CV analysis for all as-assembled cells at various scan rates. Results are showed in Fig. 5e and Fig. S20. The Li$^+$ diffusion coefficient could be calculated with the following equation:

Fig. 5. (a) CV curves of Li–S batteries with Nb$_2$O$_{5-x}$/Ru-3DG, Nb$_2$O$_5$/Ru-3DG, and Nb$_2$O$_5$-3DG based separators at a scan rate of 0.1 mV s^{-1}. (b) Peak voltages obtained from CV curves for Nb$_2$O$_{5-x}$/Ru-3DG, Nb$_2$O$_5$/Ru-3DG, and Nb$_2$O$_5$-3DG. (c) Tafel plots of oxidation reactions of LiPSs for Nb$_2$O$_{5-x}$/Ru-3DG, Nb$_2$O$_5$/Ru-3DG, and Nb$_2$O$_5$-3DG. (d) EIS curves. (e) CV curves of batteries with Nb$_2$O$_{5-x}$/Ru-3DG, Nb$_2$O$_5$/Ru-3DG, and Nb$_2$O$_5$-3DG based separators at different scan rates. (f) Linear fitting of peak currents with oxidation peak III using Nb$_2$O$_{5-x}$/Ru-3DG, Nb$_2$O$_5$/Ru-3DG, and Nb$_2$O$_5$-3DG based separators. (g) GITT curves and (h) distribution of D$_{Li}^+$ of the Nb$_2$O$_{5-x}$/Ru-3DG. (i) Charge-discharge profiles and (j) corresponding ΔE and Q2/Q1 values of Nb$_2$O$_{5-x}$/Ru-3DG, Nb$_2$O$_5$/Ru-3DG, and Nb$_2$O$_5$-3DG based separators. (k) Rate performances of Nb$_2$O$_{5-x}$/Ru-3DG, Nb$_2$O$_5$/Ru-3DG, and Nb$_2$O$_5$-3DG at different current densities from 0.1 to 8.0 C. (l) Charge-discharge of Nb$_2$O$_{5-x}$/Ru-3DG based separator cell at different C rates.

$$I_P = (2.69 \times 10^5) n^{1.5} A D_{Li}^{0.5} v^{0.5} C_{Li} \tag{2}$$

where I$_p$ was the peak current, *n* was the electron charge number, A was to the electrode area, D was the diffusion coefficient, *v* was the sweeping rate, and C was the concentration of Li$^+$. As presented in Eq. (2), diffusion efficiencies are proportional to the peak current during redox reactions. Fig. 5f and Fig. S21 exhibit square root scan rate and peak

current density diagrams. The slope value of the fitting line for Nb$_2$O$_{5-x}$/Ru-3DG was higher than that for Nb$_2$O$_5$/Ru-3DG or Nb$_2$O$_5$-3DG, illustrating faster diffusion of Li ion and accelerated redox reaction kinetics for Nb$_2$O$_{5-x}$/Ru-3DG. It is known that diffusion coefficients calculated by the CV methods are accurate under general state-of-charge (SoC), while Li$^+$ immigration between electrodes is various [56]. Therefore, we performed galvanostatic intermittent titration technique (GITT)

measurement to further analyze diffusion coefficients based on the relationship with SoC. GITT profiles were obtained by pulsing constant current at 0.1 C for 20 min, followed by 40 min of relaxing and measurement of the potential during the reaction process (Fig. 5g and Fig. S22). The D_{Li}^+ can be calculated with the following equation [57]:

$$D_{Li^+} = \frac{4}{\pi\tau}\left(\frac{n_m V_m}{S}\right)^2\left(\frac{\Delta E_s}{\Delta E_t}\right)^2 \tag{3}$$

where τ was the current pulse, n_m was the mole number, V_m was the molar volume of the electrode, S was the electrode and electrolyte interface area, ΔE_s was the potential change during steady state, and ΔE_t was the potential change during current pulses. Representative scatter points were obtained to calculate the diffusion coefficient. Diagram relationships between normalized time and log (D_{Li}^+) were plotted as shown in Fig. 5h. The average D_{Li}^+ value for the Nb$_2$O$_{5-x}$/Ru-3DG based battery was calculated to be 5.35×10^{-9} cm^2 g^{-1}, which was higher than that of Nb$_2$O$_5$/Ru-3DG (2.34×10^{-9} cm^2 g^{-1}) or Nb$_2$O$_5$-3DG (2.13×10^{-9} cm^2 g^{-1}) based battery, indicating faster Li ion diffusion kinetics of the Nb$_2$O$_{5-x}$/Ru-3DG based battery.
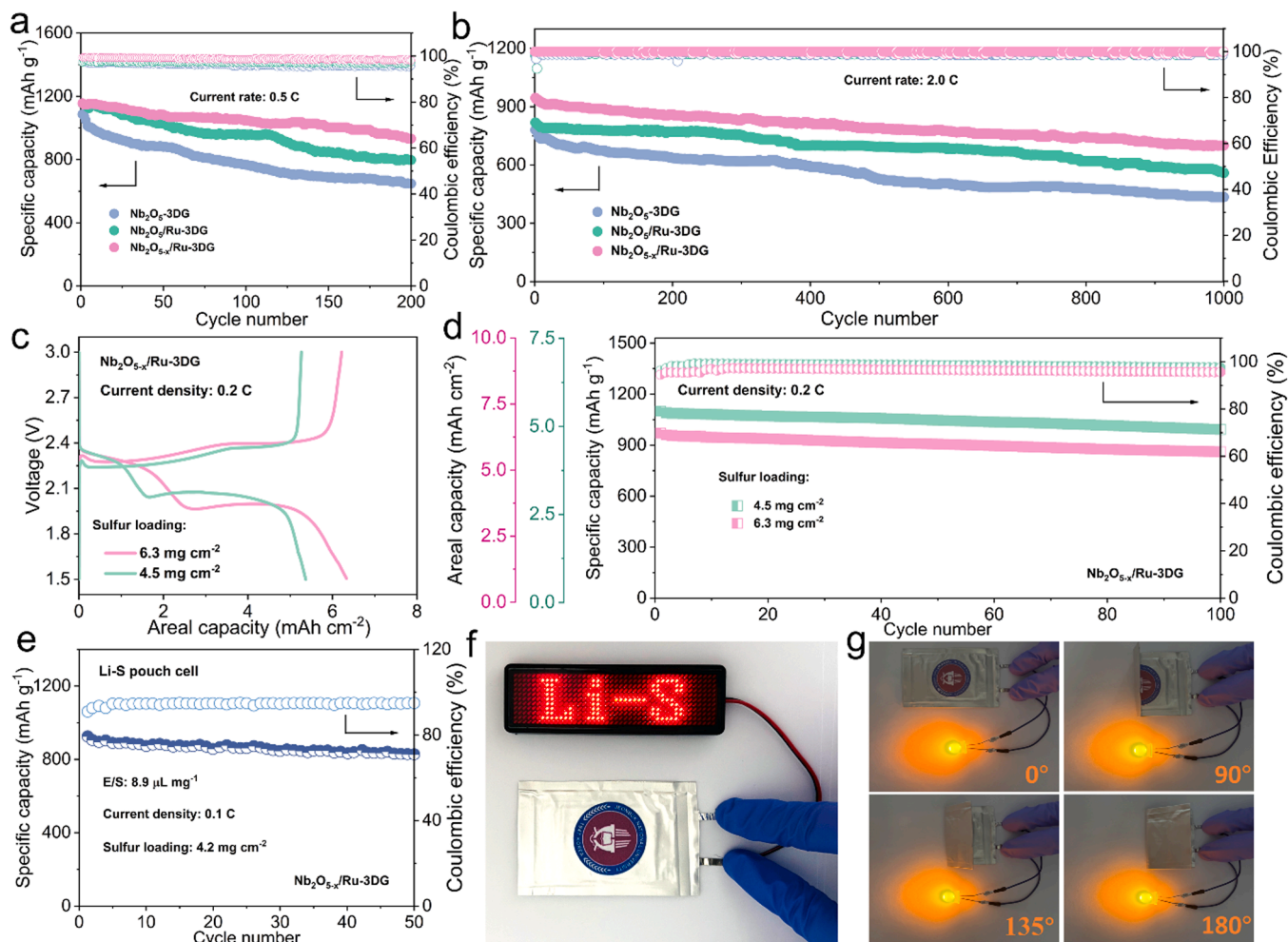
To further verify electrochemical performances of batteries using separators coated with different materials, typical galvanostatic charge/discharge curves were obtained at 0.1 C (Fig. 5i). The Nb$_2$O$_{5-x}$/Ru-3DG based battery showed a specific capacity of 1461.9 mAh g^{-1}, higher than Nb$_2$O$_5$/Ru-3DG (1343.1 mAh g^{-1}) and Nb$_2$O$_5$-3DG (1195.7 mAh g^{-1}) based batteries. Moreover, the potential difference (ΔE) between charge and discharge plateaus is an important indicator for redox reaction polarization. At a half discharge state, the Nb$_2$O$_{5-x}$/Ru-3DG based cell displayed a ΔE of 148 mV, smaller than ΔE values of Nb$_2$O$_5$/Ru-3DG (206 mV) and Nb$_2$O$_5$-3DG (218 mV) based cells. This result further reveals that the introduction of O vacancies and Ru doping could significantly reduce polarization of the redox reaction. In addition, Q1 and Q2 capacities at different discharge states indicated transformation efficiency of LiPSs (Fig. 5i). The ratio of Q2/Q1 could be used to evaluate the liquid/solid conversion ability from sulfur to soluble Li$_2$S$_x$ ($4 \le x \le 8$) and further conversion to insoluble Li$_2$S$_2$/Li$_2$S. The higher the Q2/Q1 ratio, the better the catalytic performance. The ideal ratio of Q2/Q1 is 3, indicating perfect conversion efficiency. As shown in Fig. 5j, the Nb$_2$O$_{5-x}$/Ru-3DG based battery showed a Q2/Q1 value of 2.25, which was much higher than Q2/Q1 values of batteries using Nb$_2$O$_5$/Ru-3DG (2.19) and Nb$_2$O$_5$-3DG (1.92) based separators. This confirms that Nb$_2$O$_{5-x}$/Ru-3DG has lower polarization Nb$_2$O$_5$/Ru-3DG and Nb$_2$O$_5$-3DG, which is more favorable for a solid/liquid transformation reaction. To explore the impact of structure on the electrochemical performance, we conducted the CV and charge/discharge measurement for the materials which are synthesized without template methods. Fig. S23 displayed the inferior profiles toward the LiPS conversion reaction that support the important role of template during synthesis process.

To provide quick charging and high-power density performances, a high-rate performance is an essential requirement. Therefore, we examined rate performances of all as-assembled batteries by performing charge/discharge measurements at various current densities from 0.1 to 8 C and back to 0.1 C for 10 cycles each step (Fig. 5k). Impressively, the Nb$_2$O$_{5-x}$/Ru-3DG based battery delivered a high average discharge capacity of 533.2 mAh g^{-1} even at a super high rate of 8 C, which was superior to Nb$_2$O$_5$/Ru-3DG (361.8 mAh g^{-1} at 8 C) and Nb$_2$O$_5$-3DG (260.6 mAh g^{-1} at 8 C). This excellent result might be due to its better electron/ion transport, improved charge transfer, and excellent ion diffusion capability. As the current density returned to 0.1 C, the average discharge capacity was recovered up to 1221.3 mAh g^{-1}, exhibiting excellent redox reaction reversibility. However, Nb$_2$O$_5$/Ru-3DG and Nb$_2$O$_5$-3DG based cells only delivered average recovered capacities of 1031.9 and 925.5 mAh g^{-1}, respectively. They suffered a rapid capacity decay with an increase of current rate. Fig. 5l and Fig. S24 showed typical operational charge/discharge curves of Nb$_2$O$_{5-x}$/Ru-3DG, Nb$_2$O$_5$/Ru-3DG, and Nb$_2$O$_5$-3DG based batteries at different current densities. Notably, even at a high current rate of 8 C, the Nb$_2$O$_{5-x}$/Ru-3DG based battery still presented well-defined discharge plateaus with the lowest polarization potential, evidencing its favorable stability and high-rate capability. In contrast, Nb$_2$O$_5$/Ru-3DG and Nb$_2$O$_5$-3DG based batteries at high current densities failed to show obvious discharge plateau with severe polarization due to their sluggish conversion kinetics.

Fig. 6a displays cyclic performances of batteries based on Nb$_2$O$_{5-x}$/Ru-3DG, Nb$_2$O$_5$/Ru-3DG, and Nb$_2$O$_5$-3DG separators at a current density of 0.5 C. The Nb$_2$O$_{5-x}$/Ru-3DG based cell exhibited an initial specific capacity of 1156.2 mAh g^{-1} and remained a high specific capacity value of 932.6 mAh g^{-1} after 200 cycles, showing a low decay rate of 0.096% per cycle. These results obviously surpassed results of Nb$_2$O$_5$/Ru-3DG (797.1 mAh g^{-1}; 0.148%) and Nb$_2$O$_5$-3DG (648.4 mAh g^{-1}; 0.201%) based cells. Notably, the Nb$_2$O$_{5-x}$/Ru-3DG separator-based battery achieved a high Coulombic efficiency (CE) of nearly 100%, which was superior to Nb$_2$O$_5$/Ru-3DG and Nb$_2$O$_5$-3DG based cells during a long-cycle process. This indicates that the optimal Nb$_2$O$_{5-x}$/Ru-3DG structure with enriched O vacancies and Ru heteroatom doping are beneficial for stabilization of redox reactions. Moreover, long-term stability performances of all as-assembled cells were determined at a higher current rate of 2 C (Fig. 6b). After 1000 consecutive cycles, the Nb$_2$O$_{5-x}$/Ru-3DG based cell maintained a reversible discharge capacity of 700.3 mAh g^{-1}, corresponding to a lower capacity attenuation rate of 0.025% per cycle and a high CE of 99%. In contrast, batteries with Nb$_2$O$_5$/Ru-3DG and Nb$_2$O$_5$-3DG based separators displayed inferior cycle stabilities and lower discharge capacities at 2 C. These results further verify the unparalleled role of O vacancies and Ru atom doping in LiPSs immobilization and acceleration of solid-liquid-solid reaction kinetics, which could promote phase conversion to effectively enhance sulfur utilization and extend cycle life of Li–S batteries.

To evaluate the commercialization potential of as-prepared Li–S batteries, the working performance of a cell at a higher sulfur loading is a critical factor for delivering a better energy density [58]. Hence, we assembled and investigated Li–S batteries with high sulfur loadings of 4.5 and 6.3 mg cm^{-2}. As shown in Fig. 6c, two distinct voltage plateaus were observed for batteries with Nb$_2$O$_{5-x}$/Ru-3DG based separators. At sulfur loadings of 4.5 and 6.3 mg cm^{-2}, areal capacities of Nb$_2$O$_{5-x}$/Ru-3DG achieved as high as 5.3 and 6.3 mAh cm^{-2} at a current density of 0.2 C, respectively, demonstrating excellent performances of these batteries at high active sulfur loads. Moreover, after 100 cycles, their areal capacities were 4.8 and 5.6 mAh cm^{-2}, respectively, illustrating attenuation rates of 0.094 and 0.112% per cycle for sulfur loadings of 4.5 and 6.3 mg cm^{-2}, respectively (Fig. 6d). To evaluate the structural stability of the material, the battery was disassembled after the cycle measurements. The FE-SEM image of Nb$_2$O$_{5-x}$/Ru-3DG shows that the 3D nanostructure before and after charge and discharge procedure (Fig. S25). The original morphology of Nb$_2$O$_{5-x}$/Ru-3DG is preserved that proves the high stability of the nanostructure during cycling measurement. As expected, the Nb$_2$O$_{5-x}$/Ru-3DG-based battery indeed provided comparable electrochemical performance and even showed advantages with those of recently reported materials with oxygen vacancies for Li–S batteries (Fig. S26). Based on the outstanding electrochemical performance of Nb$_2$O$_{5-x}$/Ru-3DG based battery under a higher sulfur loading, we assembled commercialization-level of pouch cell to demonstrate its practicality. Li-S pouch cell was assembled with sulfur loading of 4.2 mg cm^{-2} under an electrolyte/sulfur (E/S) ratio of 8.9 µL mg^{-1}. As shown in Fig. 6f, the as-assembled Li-S pouch cell with Nb$_2$O$_{5-x}$/Ru-3DG modified separator successfully power a circuit board with "Li-S" text. Moreover, the Nb$_2$O$_{5-x}$/Ru-3DG modified separator-based pouch cell exhibited an extremely high specific capacity of 925.8 mAh g^{-1} at 0.1 C. Specifically, after 50 consecutive charge/discharge cycles, the pouch cell battery retained a high specific capacity of 829.2 mAh g^{-1} (Fig. 6e). Interestingly, the flexible pouch cell using Nb$_2$O$_{5-x}$/Ru-3DG based separator could stably power LEDs at different bend angle of 0, 45, 90, or 180°, proving more possibilities for wearable

Fig. 6. (a) Cycling stability of Nb_2O_{5-x}/Ru-3DG, Nb_2O_5/Ru-3DG, and Nb_2O_5-3DG at 0.5 C. (b) Long-term cycling stability of Nb_2O_{5-x}/Ru-3DG, Nb_2O_5/Ru-3DG, and Nb_2O_5-3DG at 2.0 C. (c) Charge-discharge profiles and (d) Cycling stability at 0.2 C of Li-S batteries with Nb_2O_{5-x}/Ru-3DG based separator under high sulfur loadings. (e) Cycling stability of a pouch cell with Nb_2O_{5-x}/Ru-3DG based separator at 0.1 C. (f) The flexible pouch cell successfully lights up the "Li−S" panel. (g) Photographs of the flexible pouch cell at different folding states to stably light up LED.

electronic devices applications (Fig. 6g).

To deeply understand the enhanced electrochemical performance and shuttle effect inhibition, we performed density functional theory (DFT) calculations [59]. Nb_2O_5, Nb_2O_5/Ru, and Nb_2O_{5-x}/Ru models were built and investigated. Adsorption abilities were determined by calculating binding energies of models with various LiPSs. Fig. 7a and Fig. S27-29 shows adsorption abilities of Nb_2O_{5-x}/Ru (001), Nb_2O_5/Ru (001), and Nb_2O_5 (001) surfaces with LiPSs and their corresponding adsorption energies calculated. Adsorption energies of LiPSs (i.e., Li_2S_8, Li_2S_6, Li_2S_4, Li_2S_2, and Li_2S) on the surface of Nb_2O_{5-x}/Ru (001) were −2.33, −2.56, −1.47, −1.61, and −1.19 eV, respectively, which were much stronger than those of Nb_2O_5/Ru (001) (−1.72, −2.37, −1.28, −1.15, and −0.77 eV) and Nb_2O_5 (001) (−1.36, −1.92, −0.52, −0.66, and −0.35 eV) (Fig. 7b). Such enhanced adsorption capability can effectively immobilize the LiPSs and hinder the shuttling effect. In addition, the project density of state (PDOS) of each model and absorbed Li_2S_6 were calculated. As shown in Fig. 7c, the Nb_2O_{5-x}/Ru (001)-Li_2S_6 system showed a high DOS value at Fermi level, which was superior to Nb_2O_5/Ru-Li_2S_6 and Nb_2O_5-Li_2S_6. This result verified the electron transport enhancement of the Nb_2O_{5-x}/Ru (001)-Li_2S_6 system with enriched O vacancies and Ru heteroatom doping.
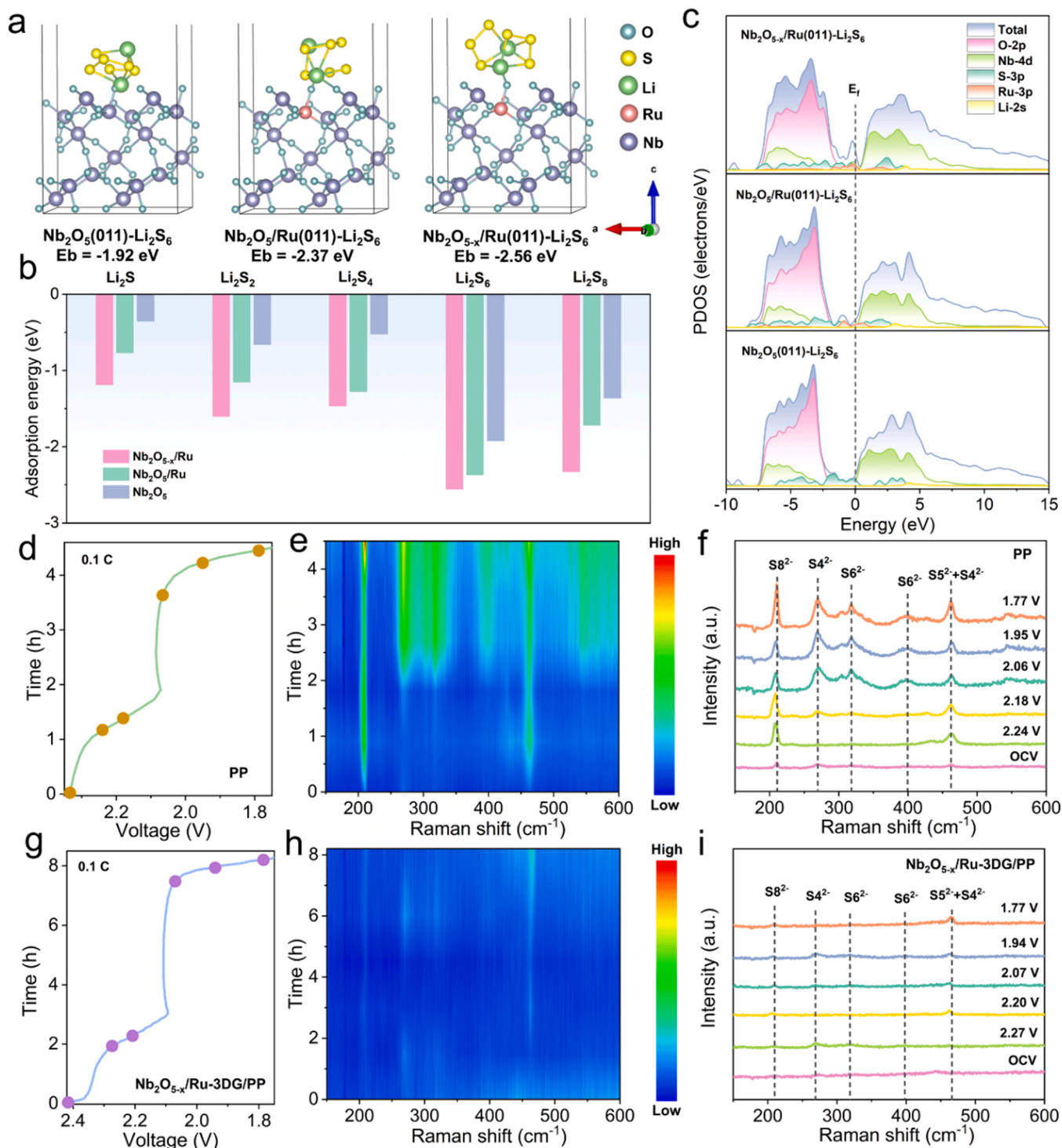
To further analyze the sulfur conversion mechanism and hinder shuttling effect ability of each modified separator, we performed in-situ Raman characterization for Nb_2O_{5-x}/Ru-3DG/PP and pristine PP

separator batteries (Fig. 7d, g). These batteries were discharged from OCV to 1.7 V to examine their conversion reaction and inhibition ability toward shuttle effect. A Raman laser was delivered to the anode side to investigate the appearance of LiPSs (Fig. S30). When the cell with pristine separator was discharged, Li_2S_8 peaks at wavelength of 208.4 cm^{-1} started to emerge at the beginning of the discharge process (2.24 V). When cells were continuously discharged, new peaks at wavelengths of 269.1, 317.4, 399.1, and 462.4 cm^{-1} appeared and maintained until the end of the discharge process. These emerged peaks were considered to be due to high-order soluble Li_2S_n ($4 \leq n \leq 6$), which might have diffused from the cathode to the anode side (shuttle effect) [60]. Conversely, corresponding soluble LiPSs peaks were absent in the cell with Nb_2O_{5-x}/Ru-3DG based separator during the whole discharge procedure (Fig. 7g-i), confirming the successful hindering the LiPSs immigration through separator.

4. Conclusions

In summary, we developed a novel method to synthesize a well-defined Nb_2O_5 with enriched O vacancies and Ru heteroatoms doping on 3D hollow graphene nanospheres (Nb_2O_{5-x}/Ru-3DG). When served as a modification layer coated on the separator for Li–S batteries, it could effectively immobilize and accelerate the conversion reaction kinetics for LiPSs, enhance the electrical conductivity, and successfully

Fig. 7. (a) Li_2S_6 adsorption on (011) surfaces of different models. (b) Comparison of adsorption energies with different LiPSs and Nb_2O_{5-x}/Ru, Nb_2O_5/Ru, and Nb_2O_5 surfaces. (c) PDOS calculation results of different models and Li_2S_6 systems. In situ Raman analyses during discharge process of (d-f) pristine PP cell, and (g-i) Nb_2O_{5-x}/Ru-3DG based separator cell.

block the shuttle effect. DFT calculations and experimental analyses confirmed that Ru heteroatom doping could stabilize O vacancies by compensating the coordination number, modulating electronic properties, and enhancing the electrocatalytic activity. Assembled $Nb_2O_5/$ Ru-3DG-based batteries delivered an excellent rate capacity of 533.2 mAh g^{-1} at 8.0 C and a long cycling stability with a small capacity attenuation rate of 0.025% per cycle at 2.0 C after 1000 cycles. More importantly, at a high S loading of 6.3 mg cm^{-2}, these batteries

exhibited excellent long-term stability by maintaining a satisfactory area capacity of 6.4 mAh cm^{-2} at 0.2 C after 100 cycles. At the industrial-level, pouch cell using Nb_2O_{5-x}/Ru-3DG coated separator displayed a high capacity of 925.8 mAh g^{-1} which was retained 829.2 mAh g^{-1} after 50 cycles, suggesting its high potential for commercialization. In summary, this study demonstrates a novel regulation strategy to prepare vacancy-induced doping that could effectively promote LiPSs adsorption and fast kinetics in Li–S batteries. It can be generalized to the field of

related energy storage systems.

CRediT authorship contribution statement

Rongrong Chu: Writing – original draft, Methodology, Investigation, Formal analysis, Data curation, Conceptualization. **Thanh Tuan Nguyen:** Validation, Supervision, Investigation, Conceptualization. **Hewei Song:** Writing – original draft, Visualization, Validation, Software, Data curation. **Yanqun Bai:** Writing – original draft, Visualization, Investigation, Data curation. **Nam Hoon Kim:** Project administration, Funding acquisition, Supervision, Writing – review & editing. **Joong Hee Lee:** Writing – review & editing, Supervision, Project administration, Funding acquisition, Conceptualization. **Duy Thanh Tran:** Conceptualization, Project administration, Writing – review & editing.

Declaration of Competing Interest

The authors declare that they have no known competing financial interests or personal relationships that could have appeared to influence the work reported in this paper.

Data availability

Data will be made available on request.

Acknowledgements

Appendix A. Supporting information

Supplementary data associated with this article can be found in the online version at doi:10.1016/j.apcatb.2024.124030.

References

[1] L. Wang, W. Hua, X. Wan, Z. Feng, Z. Hu, H. Li, J. Niu, L. Wang, A. Wang, J. Liu, X. Lang, G. Wang, W. Li, Q.-H. Yang, W. Wang, Design rules of a sulfur redox electrocatalyst for lithium–sulfur batteries, Adv. Mater. 34 (2022) 2110279.

[2] W. Guo, W. Zhang, Y. Si, D. Wang, Y. Fu, A. Manthiram, Artificial dual solid-electrolyte interfaces based on in situ organothiol transformation in lithium sulfur battery, Nat. Commun. 12 (2021) 3031.

[3] Y. Ding, Z. Shi, Y. Sun, J. Wu, X. Pan, J. Sun, Steering bidirectional sulfur redox via geometric/electronic mediator comodulation for li–s batteries, ACS Nano 17 (2023) 6002–6010.

[4] F. Zhang, Z. Tang, L. Zheng, T. Zhang, M. Xu, H. Xiao, H. Zhuang, P. Han, Q. Gao, Edge-distributed iron single-atom moiety with efficient "trapping-conversion" for polysulfides driving high-performance of Li-S battery, Appl. Catal., B 334 (2023) 122876.

[5] B. Zhang, C. Luo, Y. Deng, Z. Huang, G. Zhou, W. Lv, Y.-B. He, Y. Wan, F. Kang, Q.-H. Yang, Optimized catalytic WS2–WO3 heterostructure design for accelerated polysulfide conversion in lithium–sulfur batteries, Adv. Energy Mater. 10 (2020) 2000091.

[6] C.-C. Su, M. He, R. Amine, Z. Chen, K. Amine, The relationship between the relative solvating power of electrolytes and shuttling effect of lithium polysulfides in lithium–sulfur batteries, Angew. Chem., Int. Ed. 57 (2018) 12033–12036.

[7] W. Wang, K. Xi, B. Li, H. Li, S. Liu, J. Wang, H. Zhao, H. Li, A.M. Abdelkader, X. Gao, G. Li, A sustainable multipurpose separator directed against the shuttle effect of polysulfides for high-performance lithium–sulfur Batteries, Adv. Energy Mater. 12 (2022) 2200160.

[8] R. Chu, T.T. Nguyen, H. Song, M.A. P, Y. Bai, D.H. Kim, J.H. Lee, N.H. Kim, Crystal transformation engineering for effective polysulfides blocking layer for excellent energy density lithium–sulfur batteries, Energy Stor. Mater. 61 (2023) 102877.

[9] X. Tian, C. Yan, J. Kang, X. Yang, Q. Li, J. Yan, N. Deng, B. Cheng, W. Kang, Working mechanisms and structure engineering of renewable biomass-derived materials for advanced lithium-sulfur batteries: a review, ChemElectroChem 9 (2022) e202100995.

[10] Y. Liu, Y. Barnscheidt, M. Peng, F. Bettels, T. Li, T. He, F. Ding, L. Zhang, A biomass-based integral approach enables li-s full pouch cells with exceptional power density and energy density, Adv. Sci. 8 (2021) 2101182.

[11] J. He, A. Bhargav, H. Yaghoobnejad Asl, Y. Chen, A. Manthiram, 1T'-ReS2 nanosheets in situ grown on carbon nanotubes as a highly efficient polysulfide electrocatalyst for stable li–s batteries, Adv. Energy Mater. 10 (2020) 2001017.

[12] P. Xia, S. Li, L. Yuan, S. Jing, X. Peng, S. Lu, Y. Zhang, H. Fan, Encapsulating CoRu alloy nanocrystals into nitrogen-doped carbon nanotubes to synergistically modify lithium-sulfur batteries separator, J. Membr. Sci. 694 (2024) 122395.

[13] J. Xiong, X. Liu, P. Xia, X. Guo, S. Lu, H. Lei, Y. Zhang, H. Fan, Modified separators boost polysulfides adsorption-catalysis in lithium-sulfur batteries from Ni@Co hetero-nanocrystals into CNT-porous carbon dual frameworks, J. Colloid Interface Sci. 652 (2023) 1417–1426.

[14] F. Pei, L. Lin, A. Fu, S. Mo, D. Ou, X. Fang, N. Zheng, A two-dimensional porous carbon-modified separator for high-energy-density li-s batteries, Joule 2 (2018) 323–336.

[15] R. Wang, R. Wu, X. Yan, D. Liu, P. Guo, W. Li, H. Pan, Implanting single Zn atoms coupled with metallic co nanoparticles into porous carbon nanosheets grafted with carbon nanotubes for high-performance lithium-sulfur batteries, Adv. Funct. Mater. 32 (2022) 2200424.

[16] F. Dong, C. Peng, H. Xu, Y. Zheng, H. Yao, J. Yang, S. Zheng, Lithiated sulfur-incorporated, polymeric cathode for durable lithium–sulfur batteries with promoted redox kinetics, ACS Nano 15 (2021) 20287–20299.

[17] M. Sun, X. Wang, Y. Li, Z. Zhao, J. Qiu, Selective catalytic oxidation of pollutant H2S over Co-decorated hollow N-doped carbon nanofibers for high-performance Li-S batteries, Appl. Catal., B 317 (2022) 121763.

[18] P. Wan, S. Dong, J. Xiong, X. Jin, S. Lu, Y. Zhang, H. Fan, Synergistic catalytic conversion and chemisorption of polysulfides from Fe/Fe3C/FeN0.0324 nanocubes modified separator for advanced Li-S batteries, J. Colloid Interface Sci. 650 (2023) 582–592.

[19] J. Cai, Z. Sun, W. Cai, N. Wei, Y. Fan, Z. Liu, Q. Zhang, J. Sun, A robust ternary heterostructured electrocatalyst with conformal graphene chainmail for expediting bi-directional sulfur redox in li–s batteries, Adv. Funct. Mater. 31 (2021) 2100586.

[20] B. Yu, D. Chen, Z. Wang, F. Qi, X. Zhang, X. Wang, Y. Hu, B. Wang, W. Zhang, Y. Chen, J. He, W. He, Mo2C quantum dots@graphene functionalized separator toward high-current-density lithium metal anodes for ultrastable Li-S batteries, Chem. Eng. J. 399 (2020) 125837.

[21] Y. Bai, T.T. Nguyen, R. Chu, N.H. Kim, J.H. Lee, Core-shell hollow nanostructures as highly efficient polysulfide conversion and adsorption cathode for shuttle-free lithium-sulfur batteries, Chem. Eng. J. 454 (2023) 140338.

[22] Y. Bai, T.T. Nguyen, R. Chu, H. Song, N.H. Kim, J.H. Lee, Heterostructured TiN/TiO2 on the hierarchical N-doped carbon for enhancing the polysulfide immobilization and sulfur reduction in lithium-sulfur battery, Chem. Eng. J. 476 (2023) 146581.

[23] H. Wang, W. Zhang, J. Xu, Z. Guo, Advances in polar materials for lithium–sulfur batteries, Adv. Funct. Mater. 28 (2018) 1707520.

[24] J. Wu, T. Ye, Y. Wang, P. Yang, Q. Wang, W. Kuang, X. Chen, G. Duan, L. Yu, Z. Jin, J. Qin, Y. Lei, Understanding the catalytic kinetics of polysulfide redox reactions on transition metal compounds in Li–S batteries, ACS Nano 16 (2022) 15734–15759.

[25] J. Xu, T. Lawson, H. Fan, D. Su, G. Wang, Updated metal compounds (MOFs, −S, −OH, −N, −C) used as cathode materials for lithium–sulfur batteries, Adv. Energy Mater. 8 (2018) 1702607.

[26] P. Wan, X. Peng, S. Dong, X. Liu, S. Lu, Y. Zhang, H. Fan, Synergistic enhancement of chemisorption and catalytic conversion in lithium-sulfur batteries via Co3Fe7/Co5.47N separator mediator, J. Colloid Interface Sci. 657 (2024) 757–766.

[27] R. Chu, T.T. Nguyen, Y. Bai, N.H. Kim, J.H. Lee, Uniformly controlled treble boundary using enriched adsorption sites and accelerated catalyst cathode for robust lithium–sulfur batteries, Adv. Energy Mater. 12 (2022) 2102805.

[28] Z. Shi, Z. Sun, J. Cai, X. Yang, C. Wei, M. Wang, Y. Ding, J. Sun, Manipulating electrocatalytic Li2S redox via selective dual-defect engineering for li–s batteries, Adv. Mater. 33 (2021) 2103050.

[29] Z. Li, Q. Zhang, L. Hencz, J. Liu, P. Kaghazchi, J. Han, L. Wang, S. Zhang, Multifunctional cation-vacancy-rich ZnCo2O4 polysulfide-blocking layer for ultrahigh-loading Li-S battery, Nano Energy 89 (2021) 106331.

[30] H. Li, R. Gao, B. Chen, C. Zhou, F. Shao, H. Wei, Z. Han, N. Hu, G. Zhou, Vacancy-rich MoSSe with sulfiphilicity–lithiophilicity dual function for kinetics-enhanced and dendrite-free li-s batteries, Nano Lett. 22 (2022) 4999–5008.

[31] H. Zhang, L. Yang, P. Zhang, C. Lu, D. Sha, B. Yan, W. He, M. Zhou, W. Zhang, L. Pan, Z. Sun, MXene-Derived TinO2n−1 quantum dots distributed on porous carbon nanosheets for stable and long-life li–s batteries: enhanced polysulfide mediation via defect engineering, Adv. Mater. 33 (2021) 2008447.

[32] Y. Tian, G. Li, Y. Zhang, D. Luo, X. Wang, Y. Zhao, H. Liu, P. Ji, X. Du, J. Li, Z. Chen, Low-bandgap Se-deficient antimony selenide as a multifunctional polysulfide barrier toward high-performance lithium–sulfur batteries, Adv. Mater. 32 (2020) 1904876.

[33] S. Qiao, Q. Wang, D. Lei, X. Shi, Q. Zhang, C. Huang, A. Liu, G. He, F. Zhang, Oxygen vacancy enabled fabrication of dual-atom Mn/Co catalysts for high-performance lithium–sulfur batteries, J. Mater. Chem. A 10 (2022) 11702–11711.

[34] H. Wang, C. Xu, X. Du, G. Liu, W. Han, J. Li, Ordered porous metal oxide embedded dense carbon network design as high-performance interlayer for stable lithium-sulfur batteries, Chem. Eng. J. 471 (2023) 144338.

[35] H. Elangovan, M. Barzilay, J. Huang, S. Liu, S. Cohen, Y. Ivry, Engineering individual oxygen vacancies: domain-wall conductivity and controllable topological solitons, ACS Nano 15 (2021) 13380–13388.

[36] K. Zou, X. Chen, W. Jing, X. Dai, P. Wang, Y. Liu, R. Qiao, M. Shi, Y. Chen, J. Sun, Y. Liu, Facilitating catalytic activity of indium oxide in lithium-sulfur batteries by controlling oxygen vacancies, Energy Storage Mater. 48 (2022) 133–144.

[37] Y. Zhang, L. Feng, W. Zhan, S. Li, Y. Li, X. Ren, P. Zhang, L. Sun, Co3O4 hollow porous nanospheres with oxygen vacancies for enhanced Li–O2 batteries, ACS Appl. Energy Mater. 3 (2020) 4014–4022.

[38] Z. Li, C. Zhou, J. Hua, X. Hong, C. Sun, H.-W. Li, X. Xu, L. Mai, Engineering oxygen vacancies in a polysulfide-blocking layer with enhanced catalytic ability, Adv. Mater. 32 (2020) 1907444.

[39] X. Zhang, X. Liu, Y. Zeng, Y. Tong, X. Lu, Oxygen defects in promoting the electrochemical performance of metal oxides for supercapacitors: recent advances and challenges, Small Methods 4 (2020) 1900823.

[40] S. Lee, W. Jin, S.H. Kim, S.H. Joo, G. Nam, P. Oh, Y.-K. Kim, S.K. Kwak, J. Cho, Oxygen vacancy diffusion and condensation in lithium-ion battery cathode materials, Angew. Chem., Int. Ed. 58 (2019) 10478–10485.

[41] Z. Wu, T. Liao, S. Wang, J.A. Mudiyanselage, A.S. Micallef, W. Li, A.P. O`Mullane, J. Yang, W. Luo, K. Ostrikov, Y. Gu, Z. Sun, Conversion of catalytically inert 2D Bismuth oxide nanosheets for effective electrochemical hydrogen evolution reaction catalysis via oxygen vacancy concentration modulation, Nano-Micro Lett. 14 (2022) 90.

[42] S. Wang, Y. Wang, Y. Song, X. Jia, J. Yang, Y. Li, J. Liao, H. Song, Immobilizing Polysulfide via multiple active sites in W18O49 for Li-S batteries by oxygen vacancy engineering, Energy Storage Mater. 43 (2021) 422–429.

[43] L. Ma, Y. Zhang, S. Zhang, L. Wang, C. Zhang, Y. Chen, Q. Wu, L. Chen, L. Zhou, W. Wei, Integrating energy band alignment and oxygen vacancies engineering of TiO2 anatase/rutile homojunction for kinetics-enhanced li–s batteries, Adv. Funct. Mater. 33 (2023) 2305788.

[44] Q.P. Ngo, T.T. Nguyen, Q.T.T. Le, J.H. Lee, N.H. Kim, Unveiling the synergistic effect of atomic iridium modulated zirconium-doped pure phase cobalt phosphide for robust anion-exchange membrane water electrolyzer, Adv. Energy Mater. 13 (2023) 2301841.

[45] X. Yang, Q. Gao, Z. Zhao, Y. Guo, Y. Guo, L. Wang, Y. Wang, W. Zhan, Surface tuning of noble metal doped perovskite oxide by synergistic effect of thermal treatment and acid etching: a new path to high-performance catalysts for methane combustion, Appl. Catal., B 239 (2018) 373–382.

[46] A. Wang, C. Zhao, M. Yu, W. Wang, Trifunctional Co nanoparticle confined in defect-rich nitrogen-doped graphene for rechargeable Zn-air battery with a long lifetime, Appl. Catal., B 281 (2021) 119514.

[47] Y. Zhang, Y. Guo, Y. Wang, T. Peng, Y. Lu, R. Luo, Y. Wang, X. Liu, J.-K. Kim, Y. Luo, Rational design of 3D honeycomb-like SnS2 quantum dots/rGO composites as high-performance anode materials for lithium/sodium-ion batteries, Nanoscale Res. Lett. 13 (2018) 389.

[48] Y. Zheng, Z. Yao, Z. Shadike, M. Lei, J. Liu, C. Li, Defect-concentration-mediated T-Nb2O5 anodes for durable and fast-charging li-ion batteries, Adv. Funct. Mater. 32 (2022) 2107060.

[49] D. Luo, C. Ma, J. Hou, Z. Zhang, R. Feng, L. Yang, X. Zhang, H. Lu, J. Liu, Y. Li, Y. Zhang, X. Wang, Z. Chen, Integrating nanoreactor with O–Nb–C heterointerface design and defects engineering toward high-efficiency and longevous sodium ion battery, Adv. Energy Mater. 12 (2022) 2103716.

[50] D. Chen, R. Lu, Z. Pu, J. Zhu, H.-W. Li, F. Liu, S. Hu, X. Luo, J. Wu, Y. Zhao, S. Mu, Ru-doped 3D flower-like bimetallic phosphide with a climbing effect on overall water splitting, Appl. Catal., B 279 (2020) 119396.

[51] P. Guo, S. Sun, X. Shang, D. Liu, Y. Wang, Q. Liu, Y. Fu, D. He, Nb2O5/RGO Nanocomposite modified separators with robust polysulfide traps and catalytic centers for boosting performance of lithium–sulfur batteries, Small 15 (2019) 1902363.

[52] T.T. Nguyen, J. Balamurugan, H.W. Go, Q.P. Ngo, N.H. Kim, J.H. Lee, Dual-functional Co5.47N/Fe3N heterostructure interconnected 3D N-doped carbon nanotube-graphene hybrids for accelerating polysulfide conversion in Li-S batteries, Chem. Eng. J. 427 (2022) 131774.

[53] S. Hu, M. Yi, H. Wu, T. Wang, X. Ma, X. Liu, J. Zhang, Ionic-liquid-assisted synthesis of N, F, and B Co-Doped CoFe2O4−x on multiwalled carbon nanotubes with enriched oxygen vacancies for li–s batteries, Adv. Funct. Mater. 32 (2022) 2111084.

[54] B. Wang, L. Wang, B. Zhang, S. Zeng, F. Tian, J. Dou, Y. Qian, L. Xu, Niobium diboride nanoparticles accelerating polysulfide conversion and directing li2s nucleation enabled high areal capacity lithium–sulfur batteries, ACS Nano 16 (2022) 4947–4960.

[55] Z. Ye, Y. Jiang, L. Li, F. Wu, R. Chen, A High-Efficiency CoSe Electrocatalyst with hierarchical porous polyhedron nanoarchitecture for accelerating polysulfides conversion in li–s batteries, Adv. Mater. 32 (2020) 2002168.

[56] Y. Liang, H. Liu, G. Wang, C. Wang, Y. Ni, C.-W. Nan, L.-Z. Fan, Challenges, interface engineering, and processing strategies toward practical sulfide-based all-solid-state lithium batteries, InfoMat 4 (2022) e12292.

[57] Y. Lu, J.-L. Qin, T. Shen, Y.-F. Yu, K. Chen, Y.-Z. Hu, J.-N. Liang, M.-X. Gong, J.-J. Zhang, D.-L. Wang, Hypercrosslinked polymerization enabled N-doped carbon confined Fe2O3 facilitating Li polysulfides interface conversion for li–s batteries, Adv. Energy Mater. 11 (2021) 2101780.

[58] H.M. Kim, H.-H. Sun, I. Belharouak, A. Manthiram, Y.-K. Sun, An alternative approach to enhance the performance of high sulfur-loading electrodes for li–s batteries, ACS Energy Lett. 1 (2016) 136–141.

[59] R. Xiao, D. Luo, J. Wang, H. Lu, H. Ma, E.M. Akinoglu, M. Jin, X. Wang, Y. Zhang, Z. Chen, Oxidation states regulation of cobalt active sites through crystal surface engineering for enhanced polysulfide conversion in lithium–sulfur batteries, Adv. Sci. 9 (2022) 2202352.

[60] F. Ma, K. Srinivas, X. Zhang, Z. Zhang, Y. Wu, D. Liu, W. Zhang, Q. Wu, Y. Chen, Mo2N quantum dots decorated N-doped graphene nanosheets as dual-functional interlayer for dendrite-free and shuttle-free lithium-sulfur batteries, Adv. Funct. Mater. 32 (2022) 2206113.